Article

Development and Preliminary Application of Temperature Stress Test Machine for Cast-in-Place Inner Shaft Lining

Chi Zhang [1,*], Shuaishuai Wang [1], Tao Zhang [2], Dahai Li [3] and Hairui Cheng [4]

[1] State Key Laboratory for Geomechanics and Deep Underground Engineering, China University of Mining and Technology, Xuzhou 221116, China;
[2] School of Transportation and Civil Engineering, Nantong University, Nantong 226019, China;
[3] China Petroleum Pipeline Engineering Co., Ltd., Langfang 065000, China;
[4] Shanxi Zhengtong Coal Industry Co., Ltd. 713600, China
* Correspondence: zhangchi@cumt.edu.cn

Abstract: In order to study the anti-cracking performance of cast-in-place concrete inner shaft lining structure under the combined effects of temperature and constraint, this paper first developed a temperature stress test machine suitable for the shape of the inner shaft lining structure and with adjustable endpoint constraint, providing specialized experimental equipment for subsequent cast-in-place concrete inner shaft lining temperature stress simulation experiments. Then, by simulating the internal hydration heating and cooling process of the cast-in-place concrete inner shaft lining and using the temperature stress test machine to accurately control the endpoint constraint conditions of the inner shaft lining scaled model, this paper preliminarily studied the temperature, strain, and stress changes of the cast-in-place concrete inner shaft lining under the condition of 100% endpoint constraint.

Keywords: temperature stress test machine; concrete; hydration heat; shaft lining; degree of restraint

1. Introduction

Since 2000, deep soil layers, deep pore water-rich rock layers, and complex layers that have both of these have been commonly encountered while developing coal, iron, and other resources in China [1–3]. For these complex layers, the artificial freezing method is the most commonly used drilling method [4], accounting for over 90%. According to incomplete statistics, China has built over 150 vertical shafts using the freezing method in deep and complex layers in the past 20 years. The largest shaft net diameter D has reached 10.5m (Beijiang Haizi Coal Mine Auxiliary Shaft, Nalunhe No. 2 Coal Mine Secondary Shaft), the largest frozen soil layer thickness H_s has reached 754.96m (Wanfu Coal Mine Auxiliary Shaft, creating a world record), and the largest frozen bedrock depth H_d has reached 990m (Gaojiappao Coal Mine West Huifeng Shaft, creating a world record).

Preprints (www.preprints.org) | NOT PEER-REVIEWED | Posted: 16 May 2023 doi:10.20944/preprints202305.1140.v1

Fig. 1 Leaking water in the Inner shaft lining

However, these deep (freezing depth ≥400m) and large (D ≥8m) vertical shafts often suffered serious water leaks from the inner shaft lining after the frozen wall thawed, as shown in Fig. 1 [5,6]. For example, the Auxiliary Shaft of Longgu Coal Mine (D=7m, H_s=567.7m, H_d=650m), the Auxiliary Shaft of Hetaoyu Coal Mine (D=9m, H_s=214.6m, H_d=950m), and the main shaft of Gaojiapu Coal Mine (D=7.5m, H_s=26.5m, H_d=791m) have leakages of 34m³/h, 53m³/h, and 74.2m³/h respectively during construction, far exceeding the allowed values in GB 50384-2016 specification published by Ministry of Housing and Urban-Rural Development of China [7].

The vertical shaft is the throat of a mine, and its safety is crucial to the entire mine. Severe leaks in the inner shaft lining not only significantly increase the cost of grouting and water control, extend the construction period of the mine, and cause severe economic losses but also pose a significant safety threat to the mine, which may trigger major malignant accidents such as mud bursts and mine floods. From January 1st to 8th, 2017, the vertical shaft of the Auxiliary Shaft of the already-in-production Longgu Coal Mine (D =7m, H_s =567.7m, H_d =650m) leaked at depths of 382m and 418m, and the total flow of water quickly skyrocketed from an initial 6~8m³/h (containing about 5% mud and sand) to 105m³/h (containing approximately 15% to 30% mud and sand), which was extremely dangerous. According to in-site test data, about 2000m³ of mud and sand rushed into the vertical shaft before the rescue was successful. It can be seen that preventing leaks from the inner shaft lining of deep and frozen vertical shafts is important for ensuring the safety and production of the vertical shaft and the entire mine.

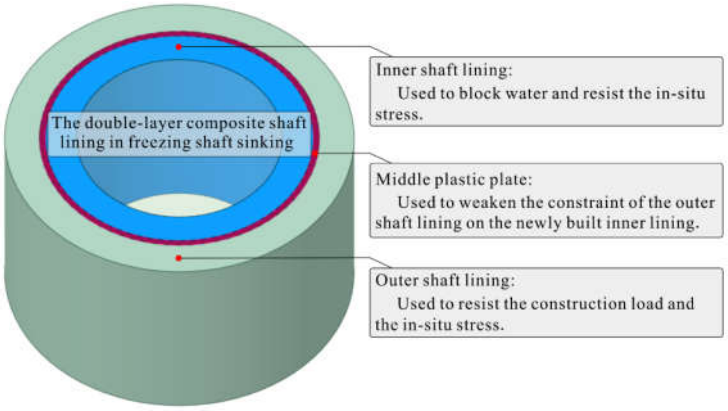

Fig. 2. Schematic of the double-layer composite shaft lining structure in the freezing shaft sinking

The above deep and large frozen vertical shaft commonly uses the double-layer reinforced concrete shaft lining structure with a sandwiched plastic plate (referred to as double-layer composite shaft lining), as shown in Fig. 2, which is widely used in the world [8,9]. Before 2000, the freezing depth of the Chinese double-layer composite shaft lining was generally less than 400m, the net diameter of the vertical shaft was rarely more than 8m, the thickness of the inner shaft lining was

 doi:10.20944/preprints202305.1140.v1

generally not more than 1m, and the concrete strength grade was not higher than C55. Currently, the sandwiched plastic plate can effectively reduce the constraint of the outer shaft lining on the newly built inner shaft lining, leading to less temperature deformation cracks of the inner shaft lining concrete [10]. Actual surveys indicate that many near-horizontal circumferential cracks gradually appear on the inner edge of the inner shaft lining with increasing vertical shaft freezing depth and diameter, as shown in Fig. 1. These cracks are the main leaky water channels of the vertical shaft, and such cracks appear even before the frozen wall thaws during construction. Theoretical analysis can exclude the possibility of inner shaft lining cracking from the points of shaft lining self-weight and formation water pressure. Preliminary judgment is that the cracking of the inner shaft lining concrete may be related to the large thickness of the inner shaft lining (up to 1m~2m) and the high-strength concrete (up to C60~C90). However, the exact failure mechanism of inner shaft lining concrete during construction is currently unclear, and there is no literature on the anti-cracking performance of cast-in-place inner shaft lining structure.

There are two dynamic processes in the freshly poured concrete: (1) the cementitious material quickly undergoes a hydration reaction, leading to an increase in concrete strength rapidly, (2) the temperature change and self-shrinkage of the concrete cause volume shrinkage, resulting in tensile damage of the concrete. Therefore, temperature change and constraint conditions are important factors affecting the concrete cracking of cast-in-place inner shaft lining during construction. The temperature change of cast-in-place inner shaft lining during construction includes two stages: (1) an initial stage where the temperature rises to the maximum temperature with the concrete hydration reaction, and (2) a later stage where the temperature gradually decreases with the influence of the frozen walls and air temperature in the vertical shaft [11]. For the inner shaft lining within a certain height range, the external constraints include the upper- and lower-end constraints and the outer circumferential surface constraint.

Existed studies have shown that the Temperature-Stress Test Machine (TSTM) is a powerful instrument for studying the early-age anti-cracking of concrete under the combined effects of temperature and constraint. TSTM can accurately control the constraint conditions of the cast-in-place concrete specimens and simulate the tensile damage and cracking process of concrete [12–15]. Riding et al. [16] used a rigid cracking frame to measure the uniaxial stress of concrete containing different fly ashes under restrained conditions, and the result showed that fly ashes reduced the cracking risk because of the decrease in the heat of hydration of the cementitious materials. Kovler [17] presented a modified uniaxial restrained shrinkage test for early-age concrete to make it possible to resolve creep strain from shrinkage strain. Shen et al. [18] used a TSTM to investigate the influence of hooked-end steel fiber and thermal treatment temperature on the early-age tensile creep of concrete under a constant tensile loading, and the result showed that the early-age autogenous shrinkage of concrete decreased with an increase of the content of hooked-end SF and increased with an increase of the thermal treatment temperature. However, studies regarding the restrained thermal and autogenous shrinkage deformations of the shaft structure remain insufficient. Additionally, most of the TSTMs with limited loading capacities are applied to low-strength concrete, which is inadequate for the shaft walls casted by high-strength concrete.

This study aims to develop a novel TSTM suitable for the shaft structure. With a similar simulation test, a preliminary investigation of the temperature, strain, and stress variations of the cast-in-place inner shaft lining under full end constraint degree (K_r = 100%) during the processes of early-age hydration heat and later cooling is studied. The constraint factor K_r refers to the degree of the end constraint of relative horizontal displacement

$$K_r = \left(X_f - X_c\right) / X_f \tag{1}$$

where X_f is the relative horizontal displacement of the inner shaft lining scaled model under unrestrained conditions at the end, and X_c is the allowed relative horizontal displacement of the scaled model. Therefore, K_r =0 means that the end of the inner shaft lining scaled model can freely expand and contract in the horizontal direction, while K_r =100% means that the allowed relative horizontal displacement of the left and right ends of the inner shaft lining scaled model is 0.

Preprints (www.preprints.org) | NOT PEER-REVIEWED | Posted: 16 May 2023 doi:10.20944/preprints202305.1140.v1

2. Test methodology

2.1. Development of the testing machine

A novel TSTM was developed to cover limitations in the loading capacity and structure style of conventional TSTMs. The TSTM consists of a restrained frame system, a slideable support system, and a measurement control system, as shown in Fig. 3. The restrained frame system is mainly formed by a rigid frame, a fixed end, and a moveable end, which are used to apply the displacement constraint from 0% to 100%. The slideable support system is used to support the weight from above, and allows horizontal displacement due to temperature dilation. The measurement control system comprises a displacement control unit, and several displacement and pressure sensors. The horizontal loading speed driven by the combination of a stepping motor and a planetary reducer (the reduction ratio is 50) ranges from 0.01 mm/min to 20 mm/min.

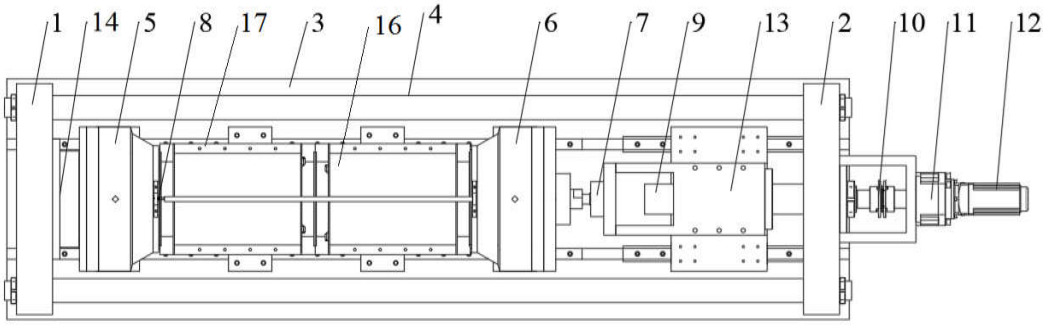

(a)

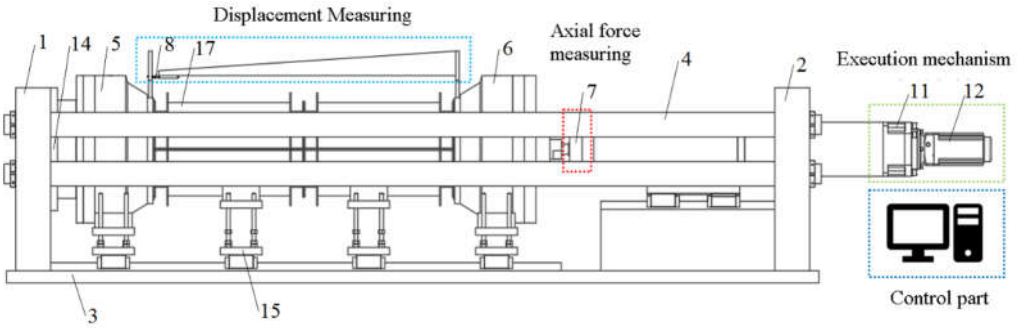

(b)

(c)

1-End bracket; 2-Supporting bracket; 3-Base plate; 4-Pull rod; 5-Fixed end clamp; 6-Movable end clamp; 7-Axial force sensor; 8-Displacement sensor; 9-Precision screw; 10-Coupling; 11-planetary reducer; 12-Stepping motor; 13-Guide component; 14-Connecting flange; 15-Slide rail support system; 16-Inner shaft lining scaled model; 17-Inner shaft lining template

Preprints (www.preprints.org) | NOT PEER-REVIEWED | Posted: 16 May 2023 doi:10.20944/preprints202305.1140.v1

Fig. 3 Schematic diagrams of the TSTM (a) top view; (b) front view; (c) physical map

In actual engineering, the net diameter of the inner wall is designed from 8 m to 10 m, and its thickness is designed from 1 m to 2 m. To achieve similarity in the model test, it is necessary for the scale test to simulate the geometry. In this study, the geometric scale ratio is taken as 40, and the ratio of height to external diameter is taken as 4, from this, the net diameter of the simulated inner wall ranges from 200 mm to 250 mm, the external diameter of the simulated inner wall ranges from 225 mm to 300 mm, and the height of the simulated inner wall ranges from 900 mm to 1200 mm. Thus, the needed minimum testing space is 1200 mm × *300 mm × 250 mm (length × width × height). Given the extra working space, the final testing space is* 2500 mm × *650 mm × 650 mm. The net diameter and the external diameter of the simulated inner wall are 200 mm and 300 mm, respectively, from which the loading capacity F of the TSTM can be calculated.*

$$F = \pi f_t \left(300^2 - 200^2\right)/4 \quad (2)$$

where f_t refers to the tensile strength of high-strength concrete C100, which is common in deep shafts. f_t equals 7.32 MPa for the steel fiber-reinforced concrete [19]. The ultimate loading capacity of the TSTM is set to 300 kN, which is slightly larger than the theoretical value. Table 1 lists the sizes of inner walls in actual engineering and model test.

Table 1. Size comparison of the engineering prototype and similar model.

Type	Geometric scale ratio	Net diameter of inner wall (mm)	Thickness of inner wall (mm)	Thickness of plastic plate (mm)	Height of inner wall (mm)
Engineering prototype	1	8000	2000	3	—
Similar model	40	200	50	0.075	1200

2.2. Temperature field measurement method of the simulated inner wall

The cubic compression strength of the conductive concrete (60 MPa) at 28 days was used in this study. A water-to-cement ratio of 0.31 was utilized for the concrete mixture. Conductive concrete reinforced with iron slag has been investigated extensively [20], and the concrete mixture proportion is listed in Table 2. P.O 52.5 cement was used, the coarse aggregate was basalt-based gravel with a size ranging from 5 mm to 10 mm, and the fine aggregate was common silica-based river sand. Generally, the internal temperature of the concrete is controlled through external heat conduction, which fails to simulate the internal hydration heat of the cast-in-place scaled model [12,21]. Research has shown that the problem of insufficient hydration heat of the cast-in-place concrete scaled model due to the reduction of the prototype structure size can be solved using the electrothermal effect [22]. The conductive concrete generates electrothermal under the action of direct current. The voltage of the direct current is adjusted according to the real-time temperature of the inner shaft lining scaled model to ensure that the temperature rise curve of the scaled model is consistent with the engineering prototype during the concrete hydration process.

Table 2. Concrete mixture proportion of simulated inner wall.

Water (kg)	Cement (kg)	Iron slag (kg)	Fine aggregate (kg)	Coarse aggregate (kg)	Water reducer (kg)
189	359	251	527	1173	1.22

2.3. Testing procedure

The TSTM testing procedure is shown in Fig. 4. First, assembling the concrete framework with the fixed and moveable ends into a whole and placing them vertically. The concrete framework was

Preprints (www.preprints.org) | NOT PEER-REVIEWED | Posted: 16 May 2023 doi:10.20944/preprints202305.1140.v1

enclosed by a heat preservation cotton, as shown in Fig. 4a. Then, a layer of polyethylene film was applied to the inside of the concrete framework to simulate the sandwiched polyethylene plate in the double-layered composite shaft, and a polypropylene pipe was fixed in the center of the concrete framework, as shown in Fig. 4b. And finally, the concrete of the inner wall was poured while burying the thermistors and fiber optic sensors, as shown in Fig. 4c and Fig. 4d. The poured concrete was placed horizontally and was fixed at both ends on the TSTM and later the displacement and stress sensors were installed, as shown in Fig. 4e. The test came to an end when the concrete temperature dropped to a minimum, or the concrete cracked during the cooling process.

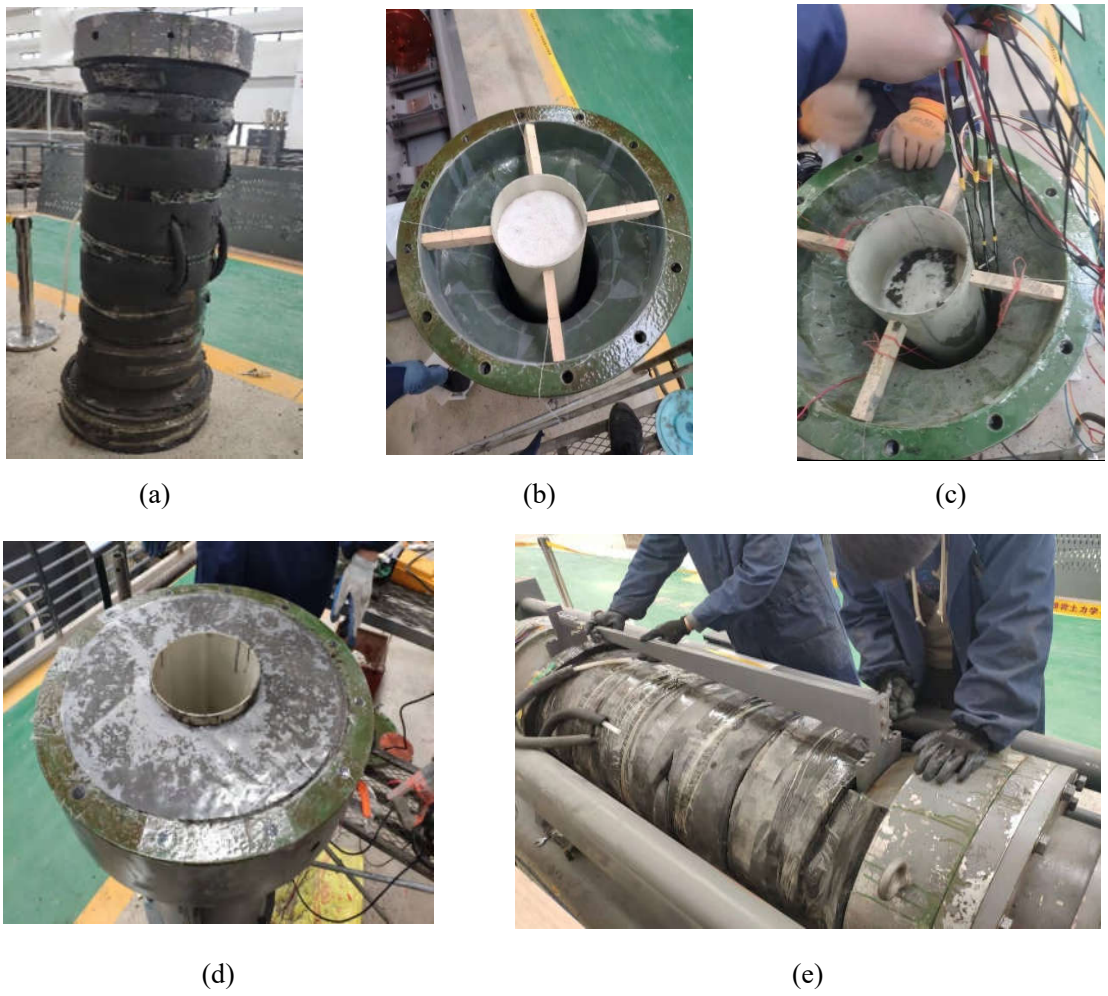

Figure 4. Testing procedure: (a) wrapping the heat preservation cotton outside the framework; (b) fixing the polypropylene pipe in the center of the concrete framework; (c) burying the thermistors and fiber optic sensors in the inner wall; (d) pouring concrete; (e) placing the concrete on the TSTM.

2.4. Sensor layout

Fig. 5 shows the layout of the thermistors and fiber optic sensors in the scaled model. The thermistors (T1~T6), buried along the radial direction of the concrete, were used to monitor the temperature variation. The fiber optic sensors (blue line in Fig. 5), placed along the inner edge of the concrete, were used to monitor the concrete strain. One monitoring point was set up at 1 cm intervals along the length of the fiber optic.

Preprints (www.preprints.org) | NOT PEER-REVIEWED | Posted: 16 May 2023 doi:10.20944/preprints202305.1140.v1

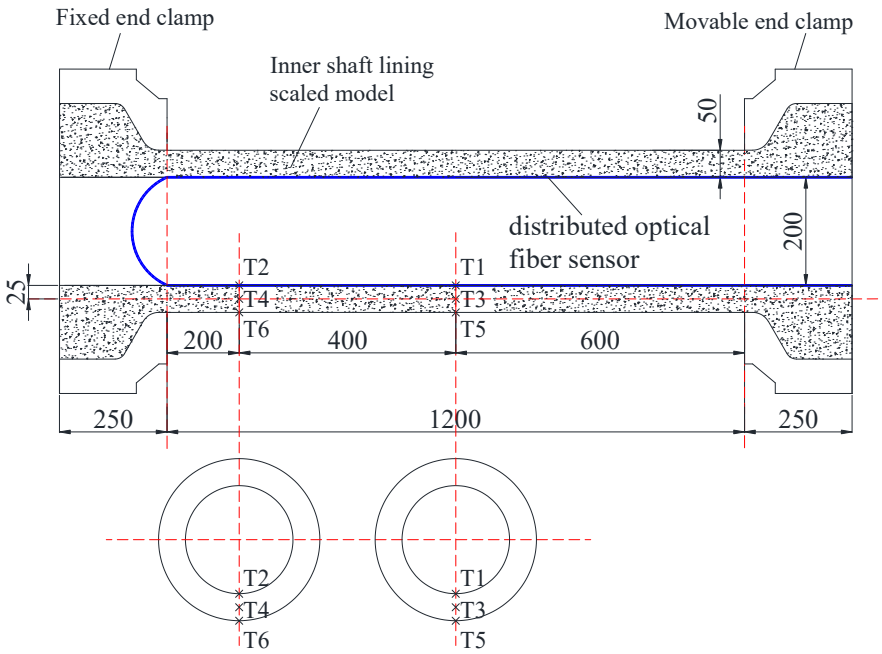

Fig. 5. Layout of the thermistors and fiber optic sensors in the scaled model

3. Results

3.1. Temperature field of the inner shaft lining scaled model

Table 3 and Fig. 6 show the temperature results and temperature variation of the shaft scaled model. The concrete entry temperature is 12.5 ℃, as shown in Fig. 6a. The results show temperature deviations between T1 and T2. For example, the deviation values are 0.60 ℃, 2.60 ℃, 2.61 ℃, 2.54 ℃, and 1.41 ℃ at the moments of 0 h, 16 h, 32 h, 51 h, and 69 h. The deviation values as a percentage of T2 are 4.5 %, 6.0 %, 6.2 %, 7.5 %, and 9.7 %, respectively. The deviation values between T3 and T4 are 0.50 ℃, 2.00 ℃, 2.15 ℃, 2.10 ℃, and 1.23 ℃, and the deviation values as a percentage of T4 are 3.9 %, 4.9 %, 5.4 %, 6.7 %, and 9.4 %, respectively. The deviation values between T5 and T6 are 0.90 ℃, 1.90 ℃, 1.87 ℃, 1.78 ℃, and 1.25 ℃, and the deviation values as a percentage of T6 are 7.2 %, 4.8 %, 4.7 %, 5.7 %, and 9.9 %, respectively. The results show that the concrete is a non-homogeneous material, and the iron slag mixed with similar material in the conductive concrete could not be homogeneous. Therefore, the shaft model cannot be heated uniformly under the electrical heat effect.

Table 3. Details of the temperature of the scaled model.

Time/h	T1 /℃	T2 /℃	T3 /℃	T4 /℃	T5 /℃	T6 /℃	T_{ave-12} /℃	T_{ave-34} /℃	T_{ave-56} /℃	T-L /℃	T-M /℃	T_{ave} /℃
0	12.7	13.3	13.2	12.7	13.4	12.5	13.0	13.0	13.0	12.8	13.1	13.0
16	40.5	43.1	42.7	40.7	41.7	39.8	41.8	41.7	40.8	41.2	41.6	41.4
32	39.8	42.4	42.3	40.2	41.4	39.6	41.1	41.2	40.5	40.7	41.2	40.9
51	31.3	33.8	33.7	31.6	33.3	31.5	32.5	32.7	32.4	32.3	32.8	32.5
69	13.1	14.5	14.3	13.1	13.9	12.6	13.8	13.7	13.3	13.4	13.7	13.6

Note: T_{ave12} = (T1+T2) / 2; T_{ave-4} = (T3+T4) / 2; T_{ave56} = (T5+T6) / 2;
T-L = (T2+T4+T6) / 3; T-M = (T1+T3+T5) / 3; T_{ave} = (T1+T2+T3+T4+T5+T6) / 6

Preprints (www.preprints.org) | NOT PEER-REVIEWED | Posted: 16 May 2023 doi:10.20944/preprints202305.1140.v1

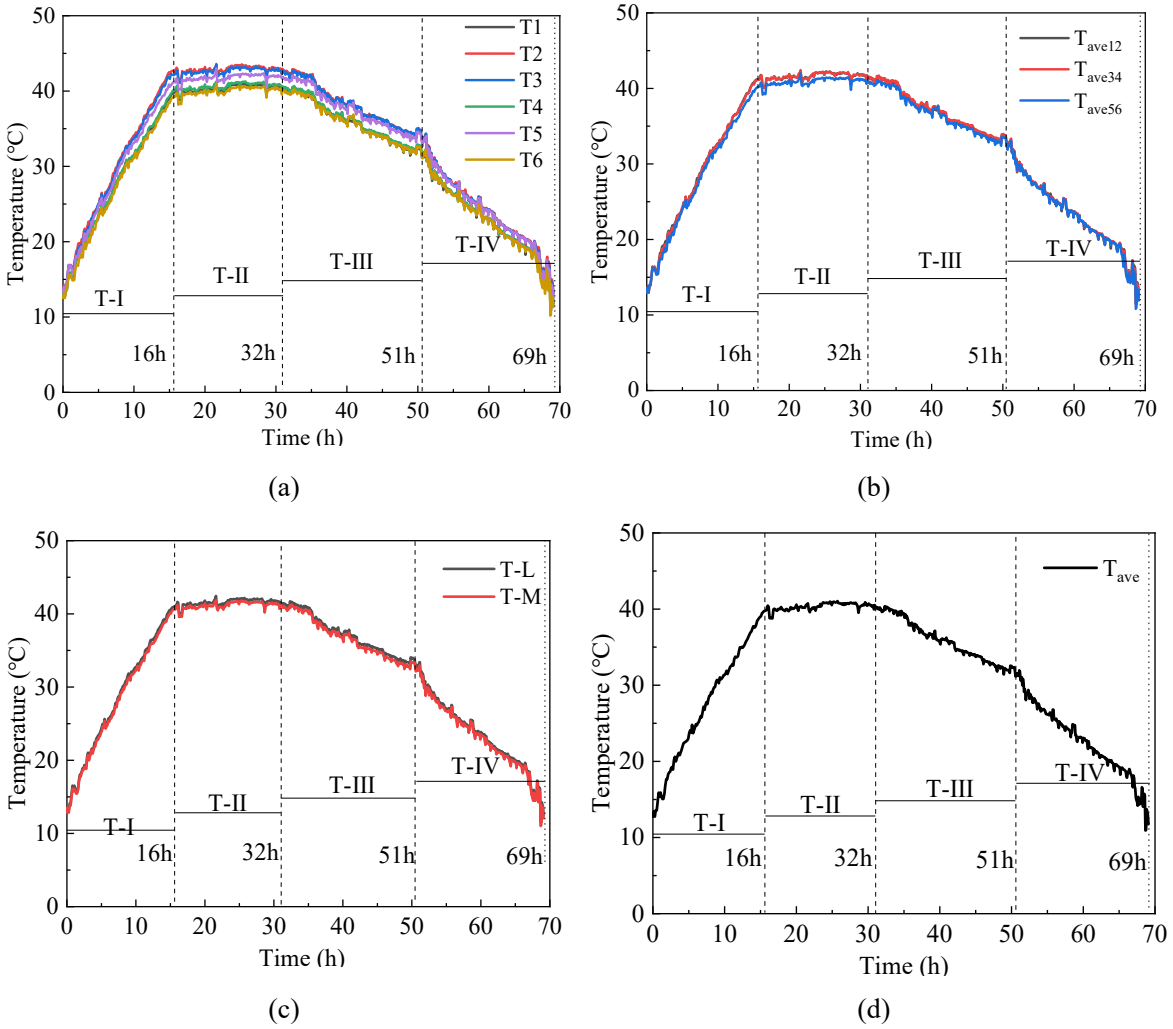

Figure 6. Temperature variation of the inner shaft lining scaled model (a) temperature at each temperature measurement point T1~T6; (b) average temperature at the scaled model inner edge T_{ave12}, middle T_{ave34}, and outer edge T_{ave56}; (c) average temperature at the fixed end cross-section T-L and middle cross-section T-M; (d) average temperature T_{ave} for T1~T6.

Fig. 6b shows the variation of the average temperatures of T_{ave12}, T_{ave34}, and T_{ave56}, respectively. The maximum difference between T_{ave12} and T_{ave34} is only 0.2 ℃. The temperature values of T_{ave12} and T_{ave34} are slightly higher than that of T_{ave56}. For example, the temperature values of T_{ave34} are higher than T_{ave56} by about 0.0 ℃, 1.0 ℃, 0.7 ℃, 0.3 ℃, and 0.4 ℃ at the moments of 0 h, 16 h, 32 h, 51 h, and 69 h, respectively. This is consistent with the pattern of a large number of field measurements, i.e., the highest temperature of the cast-in-place inner wall occurs in the middle of the inner wall off the inner edge.

Fig. 6c shows the variation of the average temperatures of the fixed end section (T-L) and the central section (T-M) of the shaft model. The maximum difference between T-L and T-M is 0.5 ℃, indicating that the temperature is relatively uniformly distributed in the height direction of the shaft model.

Fig. 6d shows the variation in the average temperature for all monitoring points. The curve can be divided into four stages: rapid heating stage (T-I), steady temperature stage (T-II), slow cooling stage (T-III), and rapid cooling stage (T-IV). In stage T-I (0~16 h), the temperature of the shaft model rises rapidly from the initial temperature of 13.0 ℃ to 41.4 ℃ with an average temperature rising rate of 1.78 ℃/h, which is attributed to the excellent conductivity under the action of 300V direct current. In stage T-II (16~32 h), the shaft model reaches thermal equilibrium with the ambient temperature of 5 ℃, and the temperature smoothly maintains at 39.8~40.5 ℃. In stage T-III (32~51 h), the concrete

Preprints (www.preprints.org) | NOT PEER-REVIEWED | Posted: 16 May 2023 doi:10.20944/preprints202305.1140.v1

strength continues to grow, and the electrical conductivity further decreases. The shaft model slowly cools down with an average cooling rate of 0.45 ℃/h. In stage T-IV (51~69 h), the shaft model rapidly cools with an average cooling rate of 1.01 ℃/h due to the low-temperature brine.

3.2. Cumulative strain

The end restraint degree K_r of the inner shaft lining scaled model in this test group is 100%, meaning that the allowed relative horizontal displacement of the two ends X_c is 0, and the displacement threshold X_t is ±5μm. Therefore, the real-time relative displacement values of the two ends of the model should be between -5μm and 5μm. In Fig. 7, the real-time relative displacement values of the model end measured are mostly between -4.2μm and 4.2μm.

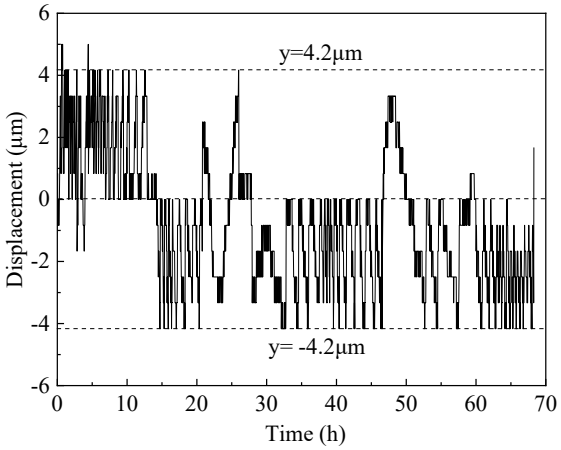

Fig. 7 Real-time relative displacement variation between both ends of the scaled model

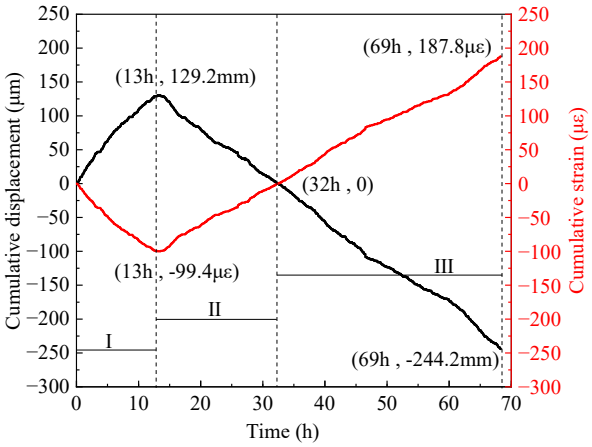

Fig. 8. Cumulative displacement and strain variations of the scaled model

Fig. 8 shows the cumulative relative displacement of the model end, which is the accumulated value of the real-time relative horizontal displacement values in Fig. 7. The change law of the cumulative relative displacement and cumulative strain of the model end can be divided into three stages: (1) the electrothermal effect of the cast-in-place conductive concrete similar material causes the inner shaft lining scaled model to undergo thermal expansion and temperature deformation from 0 to 13h. The temperature deformation is superimposed with the self-shrinkage generated by the concrete material during the hardening process, forming the volume deformation of the inner shaft lining scaled model. This is manifested in the volume deformation of the scaled model in the height direction of the inner shaft lining, that is, the cumulative relative displacement of the model end increases to the maximum value of 129.2mm at 13 hours. The cumulative relative displacement generated by the thermal expansion deformation of the model end is compressed, resulting in compressive strain in the height direction of the scaled model. Correspondingly, the cumulative strain of the inner shaft lining scaled model decreases to the maximum compressive strain of -99.4με at 13 hours; (2) the average temperature T_{ave} of the inner shaft lining scaled model remains unchanged at 39.8℃ to 40.5℃, as shown in Fig. 6, and the temperature deformation of the scaled model is not significant from 13 to 32h. The volume deformation of the inner shaft lining scaled model in the height direction is mainly composed of self-shrinkage of the concrete material. The cumulative relative displacement of the model end gradually decreases from the maximum value of 129.2mm and decreases to 0 at 32 hours, when the model height is restored to 1200mm. Correspondingly, the cumulative strain of the inner shaft lining scaled model increases from -99.4με to 0; (3) the average temperature T_{ave} of the inner shaft lining scaled model is in the slow and rapid cooling stage, as shown in Fig. 6, and the temperature deformation of the scaled model is significant from 32 to 69h. The volume deformation of the inner shaft lining scaled model in the height direction is mainly caused by temperature shrinkage deformation. The cumulative relative displacement of the model end gradually decreases to -244.2mm at 69 hours. Correspondingly, the inner shaft lining scaled model

Preprints (www.preprints.org) | NOT PEER-REVIEWED | Posted: 16 May 2023 doi:10.20944/preprints202305.1140.v1

changes from a compressed state to a tensile state, and the cumulative strain of the scaled model gradually increases to 187.8με at 69 hours.

3.3. Constraint stress

Fig. 9 shows the constrained stress of the inner shaft lining scaled model. The constrained stress is a concrete internal stress generated by the model volume deformation constrained in the vertical direction. The change in the constrained stress of the inner shaft lining scaled model can be divided into three stages: (1) the cumulative relative displacement of the model end increases to a maximum value of 129.2mm at 13 hours, as shown in Fig. 8. Correspondingly, the constrained stress of the inner shaft lining scaled model decreases to a maximum compressive stress of -2.21MPa at 13 hours; (2) the cumulative relative displacement of the model end gradually decreases from the maximum value of 129.2mm and decreases to 0 at 32 hours. Correspondingly, the constrained stress of the inner shaft lining scaled model increases to -1.22MPa at 32 hours; (3) the cumulative relative displacement of the model end gradually decreases from 0 and decreases to -244.2mm at 69 hours, as shown in Fig. 8. To achieve a constraint degree of Kr=100% for the model end, the cumulative relative displacement generated by the temperature deformation at the end should be stretched, and the constrained tensile stress at the model end gradually increases. The constrained tensile stress reaches its maximum value of 1.7MPa at 68.4 hours. Then, the constrained stress of the inner shaft lining scaled model rapidly unloads until the test completes.

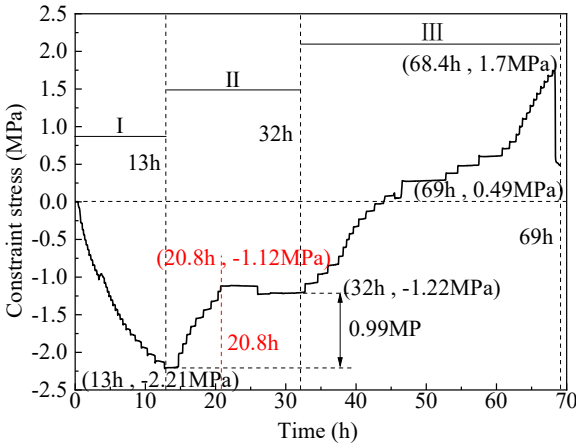

Fig. 9 Constraint stress variation of the inner shaft lining scaled model

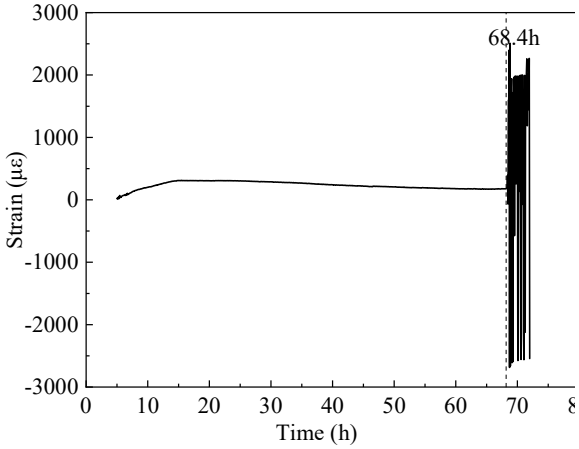

Fig. 10 Cracking time of the inner shaft lining scaled model

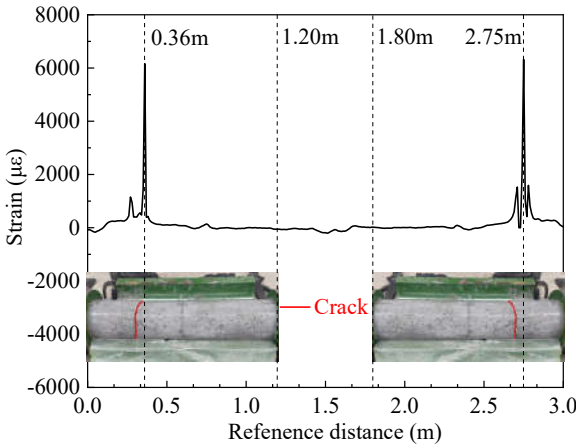

Fig. 11 Cracking location of the inner shaft lining scaled model

Fig. 10 and Fig. 11 show that the distributed fiber optic strain measurement points on the inner shaft lining scaled model exhibit a sudden increase in tensile strain and anomalous fluctuations at

 doi:10.20944/preprints202305.1140.v1

distances of 0.25m and 0.36m from the moveable end. The anomalous tensile strain values of around 6161με to 6320με far exceed the ultimate tensile strain of concrete, indicating that the inner shaft lining scaled model concrete near the moveable end clamp is under tensile cracking. After removing the model template when completing the test, it was found that the actual location where the model concrete cracked was about 0.30m away from the moveable end clamp of the scaled model.

4. Conclusion

This paper developed a novel temperature stress test machine to simulate the internal hydration heating and cooling process of cast-in-place inner shaft lining. The machine accurately controls the end constraint conditions of the inner shaft lining scaled model. The salient conclusions are summarized as follows:

(1) The average temperature at the inner edge of the inner shaft lining scaled model is close to the average temperature in the middle, and both are slightly higher than the average temperature at the outer edge of the model by 0.3℃ to 1.0℃. The temperature distribution in the height direction of the inner shaft lining scaled model is relatively uniform, with a maximum difference of 0.5℃.

(2) The average temperature variation can be divided into four stages: rapid heating stage (T-I), steady temperature stage (T-II), slow cooling stage (T-III), and rapid cooling stage (T-IV). In stage T-I (0~16 h), the temperature of the shaft model rises rapidly from the initial temperature of 13.0 ℃ to 41.4 ℃ with an average temperature rising rate of 1.78 ℃/h, which is attributed to the excellent conductivity under the action of 300V direct current. In stage T-II (16~32 h), the shaft model reaches thermal equilibrium with the ambient temperature of 5 ℃, and the temperature smoothly maintains at 39.8~40.5 ℃. In stage T-III (32~51 h), the concrete strength continues to grow, and the electrical conductivity further decreases. The shaft model slowly cools down with an average cooling rate of 0.45 ℃/h. In stage T-IV (51~69 h), the shaft model rapidly cools with an average cooling rate of 1.01 ℃/h due to the low-temperature brine.

(3) The trends in the cumulative relative displacement and cumulative strain at the end of the inner shaft lining scaled model can be divided into three stages. From 0 to 13 hours, the cumulative relative displacement at the model end increases to a maximum value of 129.2mm at 13 hours, and the cumulative strain of the inner shaft lining scaled model decreases to a maximum compressive strain of -99.4με at 13h. From 13 to 32 hours, the cumulative relative displacement of the model gradually decreases and decreases to 0 at 32 hours when the model height is restored to 1200mm, and the cumulative strain of the inner shaft lining scaled model increases from -99.4με to 0. From 32 to 69 hours, the cumulative relative displacement of the model gradually decreases and decreases to -244.2mm at 69 hours. The scaled model changes from a compressed state to a tensile state, and the cumulative strain of the model gradually increases to 187.8με at 69 hours.

(4) The change in the constrained stress of the inner shaft lining scaled model can be divided into three stages. From 0 to 13 hours, the constrained stress of the scaled model decreases to a maximum compressive stress of -2.21MPa at 13 hours. From 13 to 32 hours, the constrained compressive stress at the model end gradually transitions to tensile stress and the constrained stress of the scaled model increases to -1.22MPa at 32 hours. From 32 to 69 hours, the constrained tensile stress at the model end gradually increases, and the constrained tensile stress increases to a maximum tensile stress of 1.7MPa at 68.4 hours. Then, the constrained stress of the scaled model rapidly unloads until the test ends at 69 hours.

(5) It is feasible to determine the location and time of cracking in the scaled model by judging whether the tensile strain values at each measurement point of the distributed fiber optic sensor exceed the ultimate tensile strain of concrete. The abnormal points of the tensile strain value of the distributed fiber optic sensor are located at a distance of 0.25m and 0.36m from the movable end clamp. A certain concrete strain value near the crack of the scaled model showed a sharp increase in tensile strain at 68.4 hours.

References

1. He, M. Research progress of deep shaft construction mechanics. *Meitan Xuebao/Journal China Coal Soc.* **2021**, *46*, 726–746, doi:10.13225/j.cnki.jccs.YT21.0124.
2. Zhang, T.; Zhang, C.; Song, F.; Zou, J.; Gao, Y.; Yang, W. Breakage behavior of silica sands during high-pressure triaxial loading using X-ray microtomography. *Acta Geotech.* **2023**, doi:10.1007/s11440-023-01866-9.
3. Zhang, T.; Zhang, C.; Luo, T. Effect of stress anisotropy on deformation and particle breakage of silica sand at high-pressure compression tests. *Constr. Build. Mater.* **2022**, *316*, 125835, doi:10.1016/j.conbuildmat.2021.125835.
4. Deng, W.; Shen, J.; Qiao, G. Some problems in the construction of coal mines in western China. *Min. Eng.* **2010**, *31*, 29–33, doi:10.19458/j.cnki.cn11-2456/td.2010.04.010.
5. Yang, W. Development and prospect of freeze drilling technology in China over the past ten years. *Proc. High-Level Acad. Forum 50th Anniv. China Coal Soc.* **2012**, 1–7.
6. Cheng, H.; Cai, H. Safety Situation and Thinking about Deep Shaft Construction with Freezing Method in China. *J. Anhui Univ. Sci. Technol. Nat. Sci.* **2013**, *33*, 1–6.
7. GB-50384-2016. *Design specification for coal mine shafts and chambers*; Ministry of Housing and Urban-Rural Development of the People's Republic of China;
8. Zhou, Y.; Zhou, G.Q. Axisymmetric deformation analysis for the double layer shaft with a plastic interlayer. *Meitan Xuebao/Journal China Coal Soc.* **2010**, *35*, 1470–1475, doi:10.13225/j.cnki.jccs.2010.09.007.
9. Zhang, T.; Zhang, C.; Zou, J. Interface shear behavior of a shaft lining concrete-high density polyethylene material under different pre-imposed normal stresses. *PLoS One* **2022**, *17*, 1–17, doi:10.1371/journal.pone.0264691.
10. Zhou, J.; Zhou, G.; Shang, X.; Hu, K.; Li, T. Optimization calculation of double-layer shaft lining considering vertical additional force and temperature stress. *J. Xi'an Univ. Archit. Technol.* **2010**, *42*, 283–287, doi:10.15986/j.1006-7930.2010.02.001.
11. Zhang, T.; Yang, W.; Chen, G.; Huang, J.; Han, T.; Zhang, C. Monitoring and analysis of hydration heat temperature field for high performance mass concrete freezing shaft lining. *Caikuang yu Anquan Gongcheng Xuebao/Journal Min. Saf. Eng.* **2016**, *33*, 290–296, doi:10.13545/j.cnki.jmse.2016.02.016.
12. Nguyen, D.H.; Nguyen, V.T.; Lura, P.; Dao, V.T.N. Temperature-stress testing machine - A state-of-the-art design and its unique applications in concrete research. *Cem. Concr. Compos.* **2019**, *102*, 28–38, doi:10.1016/j.cemconcomp.2019.04.019.
13. Zhao, Z.; Zhang, H.; Fang, B.; Sun, Y.; Zhong, Y.; Shi, T. Tensile creep model of slab concrete based on microprestress-solidification theory. *Materials (Basel).* **2020**, *13*, doi:10.3390/ma13143157.
14. Kheir, J.; Klausen, A.; Hammer, T.A.; De Meyst, L.; Hilloulin, B.; Van Tittelboom, K.; Loukili, A.; De Belie, N. Early age autogenous shrinkage cracking risk of an ultra-high performance concrete (UHPC) wall: Modelling and experimental results. *Eng. Fract. Mech.* **2021**, *257*, 108024, doi:10.1016/j.engfracmech.2021.108024.
15. Estensen, A.; Terje, K.; Øyvind, K.; Sellevold, E.J. The effect of realistic curing temperature on the strength and E-modulus of concrete. *Mater. Struct.* **2018**, *51*, 1–14, doi:10.1617/s11527-018-1299-4.
16. Riding, K.A.; Poole, J.L.; Schindler, A.K.; Juenger, M.C.G.; Folliard, K.J. Quantification of effects of fly ash type on concrete early-age cracking. *ACI Mater. J.* **2008**, *105*, 149–155, doi:10.14359/19755.
17. Kovler, K. Testing system for determining the mechanical behaviour of early age concrete under restrained and free uniaxial shrinkage. *Mater. Struct.* **1994**, *27*, 324–330, doi:10.1007/BF02473424.
18. Shen, D.; Liu, C.; Kang, J.; Yang, Q.; Li, M.; Li, C.; Zeng, X. Early-age autogenous shrinkage and tensile creep of hooked-end steel fiber reinforced concrete with different thermal treatment temperatures. *Cem. Concr. Compos.* **2022**, *131*, 104550, doi:10.1016/j.cemconcomp.2022.104550.
19. Abdi Moghadam, M.; Izadifard, R.A. Prediction of the tensile strength of normal and steel fiber reinforced concrete exposed to high temperatures. *Int. J. Concr. Struct. Mater.* **2021**, *15*, doi:10.1186/s40069-021-00485-6.
20. Jiang, Y.; Ling, T.C.; Shi, C.; Pan, S.Y. Characteristics of steel slags and their use in cement and concrete—A review. *Resour. Conserv. Recycl.* **2018**, *136*, 187–197, doi:10.1016/j.resconrec.2018.04.023.
21. Li, L.; Dao, V.; Lura, P. Autogenous deformation and coefficient of thermal expansion of early-age concrete: Initial outcomes of a study using a newly-developed Temperature Stress Testing Machine. *Cem. Concr. Compos.* **2021**, *119*, 103997, doi:10.1016/j.cemconcomp.2021.103997.
22. Yin, J. Thermo-physical and mechanical properties of the similar material of inner shaft lining concrete during construction period, China University of Mining and Technology, 2020.